2019

Nanoindentation characterization on local plastic response of Ti-6Al-4V under high-load spherical indentation

Yan Wen

Lechun Xie

Zhou Wang

Liqiang Wang

Weijie Lu

See next page for additional authors

10.1016/j.jmrt.2019.06.009

Wen, Y., Xie, L., Wang, Z., Wang, L., Lu, W., & Zhang, L. C. (2019). Nanoindentation characterization on local plastic response of Ti-6Al-4V under high-load spherical indentation. *Journal of Materials Research and Technology*. Available here

Available online at www.sciencedirect.com

jmr&t Journal of Materials Research and Technology

www.jmrt.com.br

Original Article

Nanoindentation characterization on local plastic response of Ti-6Al-4V under high-load spherical indentation

Yan Wen[a,b], Lechun Xie[a,b,*], Zhou Wang[a,b], Liqiang Wang[c,d,*], Weijie Lu[c], Lai-Chang Zhang[e]

[a] Hubei Key Laboratory of Advanced Technology for Automotive Components, Wuhan University of Technology, Wuhan 430070, PR China
[b] Hubei Collaborative Innovation Center for Automotive Components Technology, Wuhan 430070, PR China
[c] State Key Laboratory of Metal Matrix Composites, School of Materials Science and Engineering, Shanghai Jiao Tong University, No. 800 Dongchuan Road, Shanghai 200240, PR China
[d] Collaborative Innovation Center for Advanced Ship and Deep-Sea Exploration, Shanghai 200240, PR China
[e] School of Engineering, Edith Cowan University, 270 Joondalup Drive, Joondalup, Perth, WA 6027, Australia

ARTICLE INFO

Article history:
Received 30 January 2019
Accepted 5 June 2019
Available online 24 June 2019

Keywords:
Nanoindentation
Spherical loading
Hardness
Microstructure
Ti-6Al-4V

ABSTRACT

After high-load spherical indentation treatment, the variations of hardness on the plastic zone of Ti-6Al-4V were investigated via nanoindentation method. The hardness within the center of plastic zone was measured by nanoindenter, and the magnitude decreased gradually along the depth, which were caused by the different extent of plastic deformation under the residual imprint. The microstructure of indentation were observed using scanning electron microscope (SEM) before and after surface etching, and the results showed that the microhardness revealed the average hardness of α and β phases of Ti-6Al-4V. The maximum hardness reached 6.438 GPa in the depth of 132 μm. In addition, the two and three dimensional contour profiles of residual imprint introduced by high-load spherical indentation were measured by the white-light interferometer and the shape of residual imprint was obtained. All results were discussed in detail.

1. Introduction

Titanium alloys have received considerable attention because of their good physical and mechanical properties [1–6]. As one kind of important titanium alloys, Ti-6Al-4V has been studied widely, including the microstructure, hardness, fatigue properties, and so on [7–10]. However, during the process of manufacturing and subsequent heat treatments, tensile stresses are always generated on the surface layer, which may deteriorate the mechanical properties of Ti-6Al-4V [11–13]. In the interest of improving the unfavorable properties, surface modification are usually utilized and surface properties are studied as well [14–16], for example, the surface plas-

* Corresponding authors.
E-mails: xielechun@whut.edu.cn (L. Xie), wang_liqiang@sjtu.edu.cn (L. Wang).
https://doi.org/10.1016/j.jmrt.2019.06.009

tic deformation and the hardness variation after spherical loading. Spherical loading is a critical factor that must be considered during the rolling contact process, which influences the rolling contact fatigue lives of components obviously [17–19]. After implementing spherical loading on a metal material, a residual imprint is usually formed, and a local plastic zone surrounds the residual imprint simultaneously. Nowadays, researchers have mostly focused on the macroscopically mechanical properties of titanium alloys [20,21]; there is little investigation related to the local mechanical properties of Ti-6Al-4V after high-load spherical indentation. Therefore, studying the local mechanical properties of plastic zone surrounding the residual imprint is significant for using Ti-6Al-4V alloy.

Generally, hardness is an important indication of mechanical properties in local plastic zone. Traditional Vickers indentation has been used to test the hardness of subsurface layer of shot-peened Ti-6Al-4V in the previous work [22]. In order to obtain the distribution of hardness along the depth in local plastic zone, the thin surface layer must be removed bit by bit via chemical etching at each depth, which makes it hard and time-consuming to accurately control the depth. Thus this method should be improved, and some references have reported that the nanoindentation method is effective to characterize the hardness [23,24], but it preliminary focuses on thin films and coating materials. In 1986, Noerner and Nix started to investigate the elastic and plastic properties of thin films by depth-sensing indentation instruments [25]. In 1989, Nix systematically studied the mechanical properties of thin films on substrates [26], and the mechanical properties of thin films required the development of nontraditional mechanical testing techniques. In 1991, Tirupataiah and Sundararajan considered the constraint factor associated with the indentation of work-hardening materials with a harder spherical ball [27], and the constraint factor was dependent on the material properties. In 1992, Pharr and Oliver indicated that the residual stresses of thin films could be measured via nanoindentation experiments [28]. In 2002, Saha and Nix examined the effects of the substrate on the determination of mechanical properties of thin films by nanoindentation [29]. In addition, some simulation work related to spherical indentation and nanoindentation has been implemented. Bhattacharya and Nix utilized the finite element method to study an elastoplastic analysis of axisymmetric conical indentation, and it was found that the shapes of the plastic zones depended strongly on both indenter angle and the ratio of Young's modulus to yield strength [30]. Furthermore, Donohue et al. [31] utilized finite element method to simulate the spherical indentation, and established the important connections between the indentation stress–strain curves and the conventional uniaxial stress–strain curves. However, in none of the studies mentioned above, has the related research about Ti-6Al-4V been involved. In 2015, Han et al. [32] utilized the crystal plasticity finite element method to simulate the load-displacement curves of Ti-6Al-4V. The simulated results indicated that the nanoindentation could introduce the plastic strain around the indentation, and the size of strain area was similar to the size of the indentation.

Additionally, some experimental work using the nanoindentation method to investigate the mechanical properties of Ti-6Al-4V has been carried out. In 2008, Li et al. [33] conducted the nanoindentation tests on the hole surface and subsurface in high-throughput drilling of Ti-6Al-4V. Nanoindentation tests identified a 15–20 μm thick of high-hardness subsurface layer with peak hardness over 9 GPa, relative to the 4–5 GPa of bulk material. In Everitt et al.'s [34] work in 2009, a nanoindentation technique was applied to measure the mechanical characteristics of the debris layer and the Ti-6Al-4V immediately below the debris layer. In 2011, Man et al. [35] investigated the hardness of the nitride layer of laser diffusion treated Ti-6Al-4V. Nanoindentation measurements revealed that the hardness of the nitride layer was around 11.3 GPa, about 2.3 times that of non-treated Ti-6Al-4V. In 2014, nanoindentation characterization on Ti-6Al-4V obtained by electron beam additive manufacturing was experimentally investigated by Gong et al. [36]. The indentation measurements identified the highest Young's modulus of 127.9 GPa and hardness of 6.5 GPa, which was attributed to the strengthening phase of α′ and fine microstructure during the process of additive manufacturing.

Dynamic indentation tests using spherical projectile was carried out on solution treated and aged Ti-6Al-4V alloy at ambient conditions in Kumaraswamy's work [37]. Hardness increased with the strain up to the critical strain, due to the localization of plastic deformation underneath the impacting ball [37]. Han et al.'s [32] experiments revealed the sensitivities of nanoindentation to the different grain orientations. Meanwhile, indentation tests were performed on Ti-6Al-4V alloy quenched at various temperatures using a Berkovich indenter in Cai's work [38], and the loading speed had little influence on measurement of hardness and Young's modulus. Hardness as well as Young's modulus were strong effected by indentation size [38]. Similar results were obtained in Dong et al.'s work [39], and the hardness decreased with the increase of the indentation load, which was caused by the effects of indentation size.

Although the nanoindentation method has been utilized to investigate the mechanical properties of Ti-6Al-4V, little investigation can be found regarding the local plastic response under high-load spherical indentation, and the determination of the depth of the local plastic zone. In this study, a useful quantification methodology of the heterogeneous plastic deformation caused by spherical indentation in Ti-6Al-4V will be provided, and the plastic deformation during spherical loading can be used in the microstructure models and simulations of similar processes. Therefore, in this work, the cylinder sample of Ti-6Al-4V will first undergo high-load spherical indentation, then the variations of hardness on the local plastic zone will be investigated via nanoindentation method. The microstructure of indentations will be observed and all variations will be discussed in detail.

2. Experimental procedures

2.1. *Preparation of materials and high-load spherical indentation*

The specimen of Ti-6Al-4V used in this study was obtained via high-temperature synthesis. Before the experiment of ball indentation, the samples was annealed at 700 °C for 2 h and

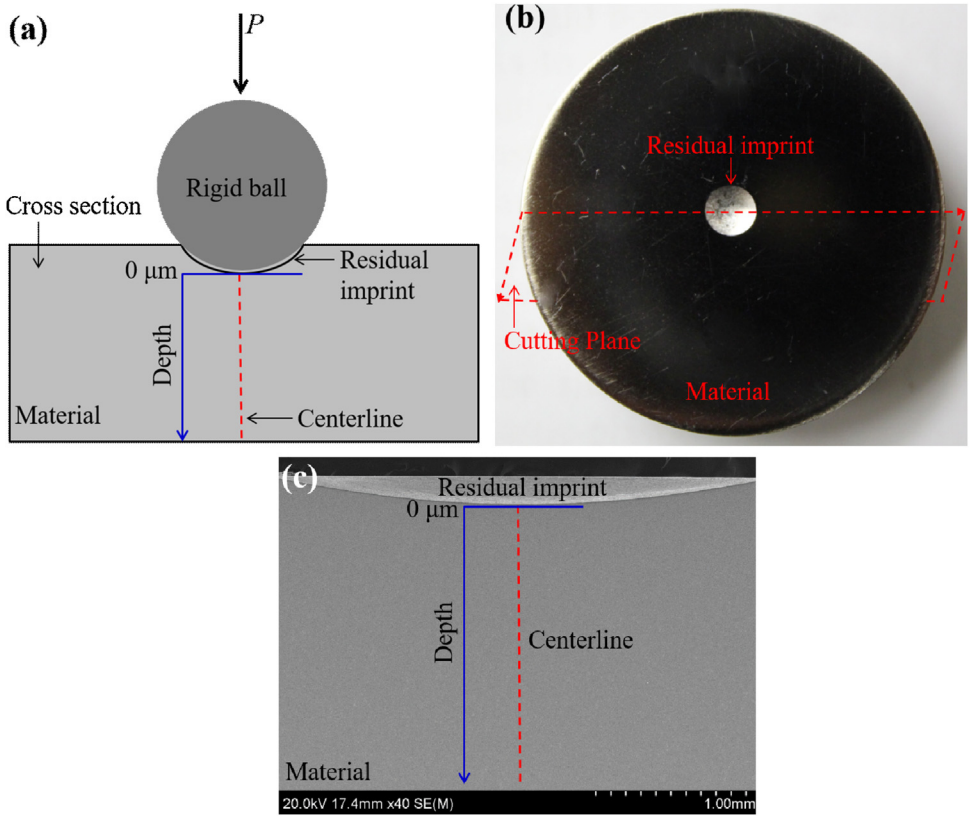

Fig. 1 – (a) Schematic process of spherical loading; (b) Photos of the sample and the residual imprint after loading; (c) SEM image of the cross-section.

then removed the oxide layer on surface by sanding. The microstructure of etched surface is shown in the following SEM images in the part of results and discussion, and it can be found that the α (gray, online) and β (white, online) phases are distributed uniformly. And most of phases are α. Because Ti-6Al-4V contained two phases of α and β, for obtaining the uniform distribution of two phases, the manufacturing process of melting and annealing were introduced. The diameter of sample was 3 cm and the thickness was 1 cm. The high-load spherical indentation was done using hydraulic pressure equipment with a 52,100 steel ball ($D = 0.5$ in.) as the rigid ball, and the residual imprint formed. The magnitude of loading (P) was about 2×10^4 N and the dwell time was 1 min. Before implementing the spherical loading, the surface of the cylindrical sample was orderly ground using three kinds of abrasive papers (400 + 600 + 800 grit) firstly, and then polished using 9 μm diamond suspensions. Because the spherical loading would introduce large plastic deformation on the surface, there is no need of the further surface polishing. The schematic process of spherical loading is shown in Fig. 1(a), and the photos of the sample and the residual imprint after loading are displayed in Fig. 1(b). Labels for the zero point and the direction of increasing depth are added to Fig. 1(a) and (c), the schematic figure of the cutting plane is shown in Fig. 1(b), and the scanning electron microscope (SEM) image of the cross-section is displayed in Fig. 1(c).

2.2. *Microstructure observation*

The microstructure observation included two parts: (1) the two and three dimensional contours of residual imprint were obtained via using the white-light interferometer (ADE Phase Shift, USA); (2) the microstructure of indentations on the cross-section were observed using SEM (Hitachi S-4800, Japan) with a voltage of 20 kV before and after surface etching. During the experiment, the sample was cut along the diameter by the cutting machine with an external diamond blade, and the thickness of blade was 0.3 mm. In order to reduce the modification of plastic zone, the cutting speed was slow and the cooling liquid was utilized to decrease the heat concentration. Before grinding and polishing, the cold mounting method was utilized to avoid the influence of heating during the process of mounting. After mounting, in part (2), standard metallographic grinding and polishing procedures were used before observation. The cross-section was ground using different abrasive papers (400 + 600 + 800 grit) over a short time, and polished using 9 and 3 μm diamond suspensions, and then 0.05 μm aluminum oxide suspension in that order. Because the grinding and polishing time were short, the influence on plastic zone was reduced to the minimum. In addition, in order to observe the phases of Ti-6Al-4V, the surface of sample was etched using Kroll's Solution ($HF : HNO_3 : H_2O = 3 : 5 : 100$) for 2–4 s, then cleaned with deionized water and acetone before SEM observation.

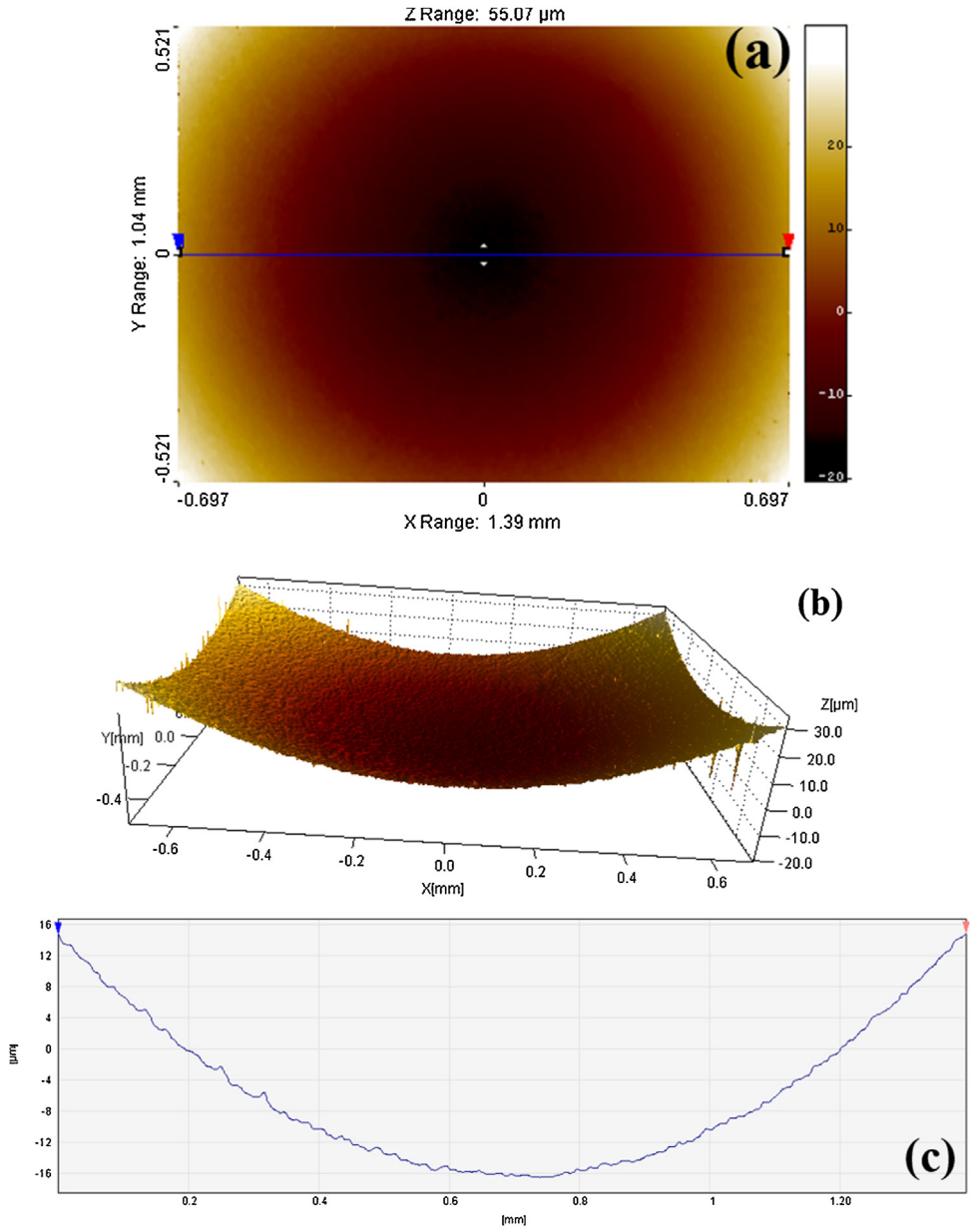

Fig. 2 – Two and three dimensional contours of the residual imprint after the spherical loading: (a) the two dimensional contour; (b) the three dimensional contour; (c) the line contour.

2.3. *Measurements on hardness and reduced modulus*

Before testing by the nanoindentation method, the tests by traditional Vickers indentation were first implemented in the center underneath the residual imprint. Vickers hardness was measured by a Digital Hardness Tester (DHV-1000, Beijing, China) with loading weight of 2.94 N and holding time of 20 s. The distance between two adjacent indentations was 100 μm. Afterwards, the measurement of hardness and reduced modulus were taken via the nanoindentation method utilizing nanoindenters (Micro Materials Ltd., UK). The Berkovich indenter, a three-sided pyramid with an area-to-depth function was used in all measurements. During tests, the indenter geometry shape factor was 1.0. The maximum load was 50 mN and the loading rate was 1 mN/s. The dwell time with maximum load was 30 s. In order to measure the variation of hardness and the reduced modulus along the depth, ten locations were tested in order from the bottom of residual imprint. The accurate distance between two adjacent locations was measured. At each location, four indentations were made to reduce measurement error. All measurements were implemented at room temperature.

3. Results and discussion

3.1. *Microstructure observation*

Fig. 2 shows the two and three dimensional contours of the residual imprint after high-load spherical indentation. The two dimensional optical contour of residual imprint is presented in Fig. 2(a), and it can be seen that the profile is a circle.

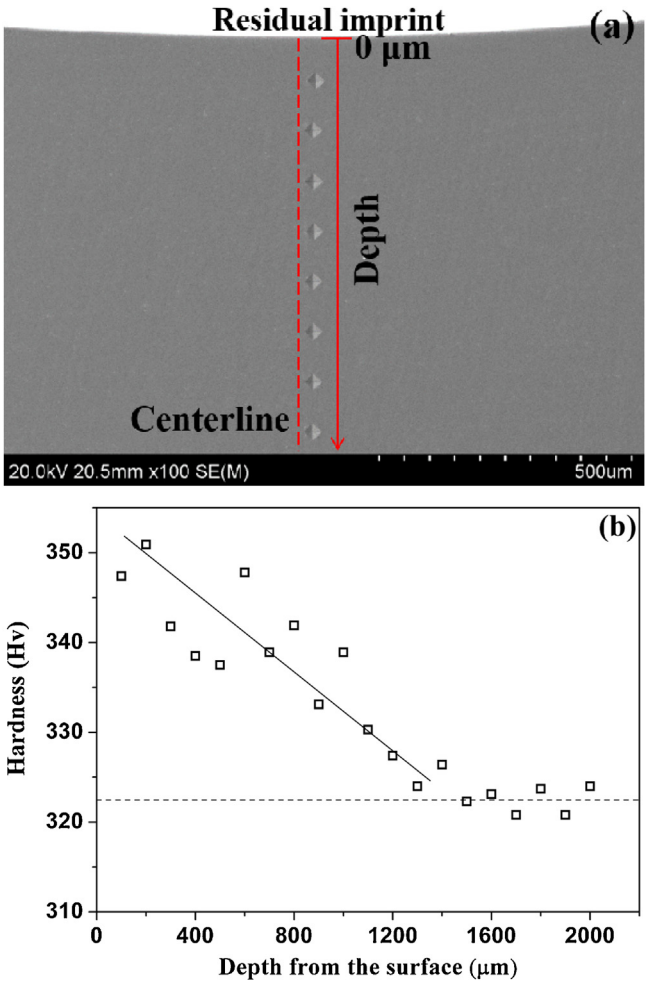

Fig. 3 – (a) SEM image of Vickers indentations along the centerline starting from the bottom of the residual imprint; (b) Distribution of Vickers hardness.

The three dimensional contour and the line contour of residual imprint are shown in Fig. 2(b) and (c), respectively, where the depth of residual imprint is estimated as 32 μm. According to the diameter and depth of residual imprint, the compressed volume of material is about 0.0408 mm^3 after high-load spherical indentation, due to the plastic deformation by the pressure and extrusion of 52,100 steel ball during the process of spherical loading [40,41].

Before testing by the nanoindentation method, the tests by traditional Vickers indentation are implemented and the test results are shown in Fig. 3. Fig. 3(a) shows the SEM image of Vickers indentations along the centerline starting from the bottom of the residual imprint. From the results in Fig. 3(b), the coarse tendency can be found that with the increasing of depth, the hardness decreases directly and then reaches a minimum low of about 320 Hv. However, it is hard to derive the detailed trends and rules on the aspect of hardness variation from the Vickers hardness, especially in the area close to the residual imprint. In addition, the hardness obtained from Vickers indentation is obviously observed to be discrete. Therefore, in order to obtain the accurate trends and rules of hardness variation, and the relationship between hardness and plastic zone, the nanoindentation method is introduced as an effective method for characterization.

Due to the disadvantages of measuring hardness using Vickers indentation, the hardness underneath the residual imprint are tested at various depths along the centerline via nanoindentation method, and the SEM images of indentations before and after surface etching are shown in Fig. 4

. Four indentations in each location are shown clearly in the center, and the magnification of four indentations are illustrated in Fig. 4(a) and (b). Distance from the surface is labeled in the figure. Moreover, the accurate distance between two adjacent locations are labeled and shown in Fig. 4(c). In 2015, Han et al. [32] utilized the crystal plasticity finite element method for simulating the load–displacement curves, which agreed with the experimental data. Their simulated results indicated that the nanoindentation introduced the plastic strain around the indentation, and the size of strain area was similar to the size of the indentation. In order to avoid the influence of residual strain between two adjacent indentations and assure the accuracy of measurement, the distance between two indentations is at least double of the indentation size. Therefore, based on the expected size of indentations, the distance between two adjacent indentations is set at 15 μm in this work. In addition, based on calculation, using more indentations in each location will lead to excessive coverage area, which will influence the accuracy of measurement area. For instance, using 9 indentations will make the coverage area reach at least 900 μm^2 in each location, which has been shown in the schematic picture in Fig. 4(d). Considering both factors, using 4 indentations to determine the hardness in each location is appropriate for this study, as the accuracy of the measurement of hardness in smaller coverage area can be ensured. The schematic pictures of the distance between two adjacent locations and the coverage area by indentations are shown in Fig. 4(d).

The four indentations represent four measurements in each location, and four load-displacement curves can be obtained. In Fig. 4(a), by comparing the indentation size between location 1 and 4, it is shown that the size of indentation in location 1 is smaller than that in location 4, which agrees with the determination of hardness in Fig. 5, which will be shown in the following section. The smaller size of indentation, the higher hardness. The indentation size indicates that the higher hardness exists closer to the residual imprint, which is due to the strain hardening under spherical loading [40,41]. Owing to the effect of pressure and extrusion by 52,100 steel ball, the plastic deformation is generated below and around the residual imprint.

SEM images of indentations after surface etching are shown in Fig. 4(b). From the magnification of location 1, two phases α (gray area) and β (white area) of Ti-6Al-4V can clearly be seen. After surface etching, the indentation size and the variation trend are almost the same as that before etching. Furthermore, in Fig. 4(b), the phases impacted by the indentation can clearly be observed, that is the big advantage of Fig. 4(b) compared to Fig. 4(a). The plastic deformation of α and β phases is displayed after the indentation test, as well as the indenters impact on both α and β phases, which shows that the hardness are the average values of α and β phases.

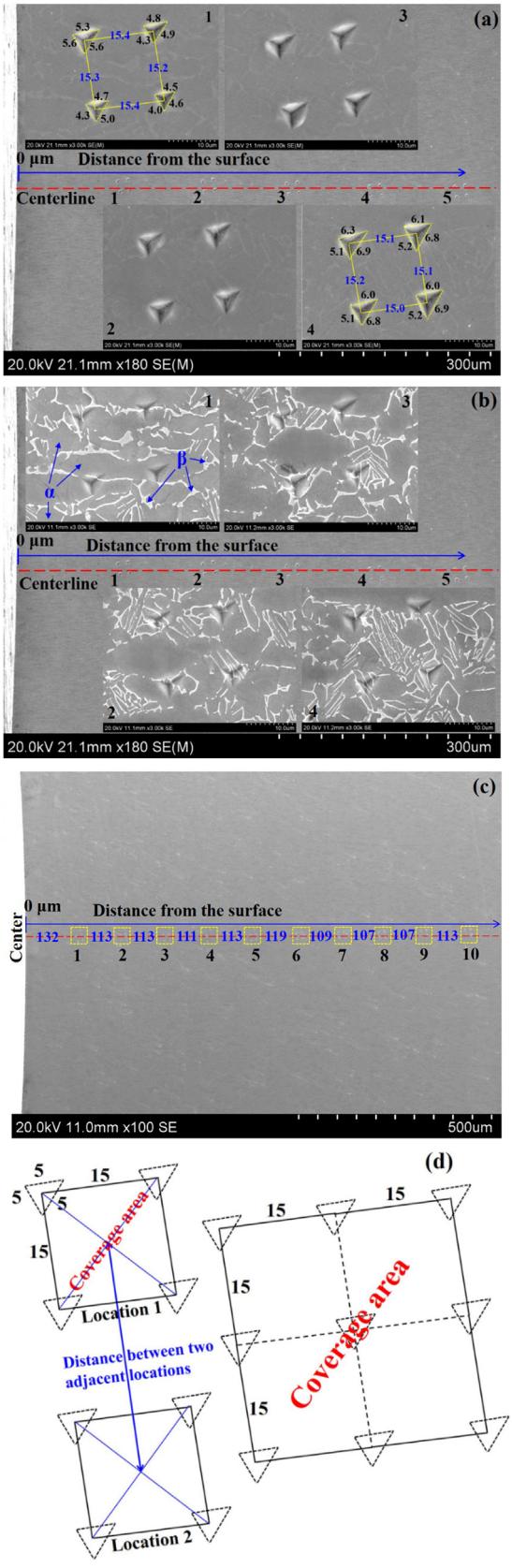

Fig. 4 – SEM images of indentations along the centerline before and after surface etching: (a) before etching; (b) after etching. The size and distance (μm) of indentations are measured and shown in (a), and the accurate distance (μm) between two adjacent locations are displayed in (c). The schematic pictures of the distance between two adjacent locations and the coverage area after tests are drawn in (d).

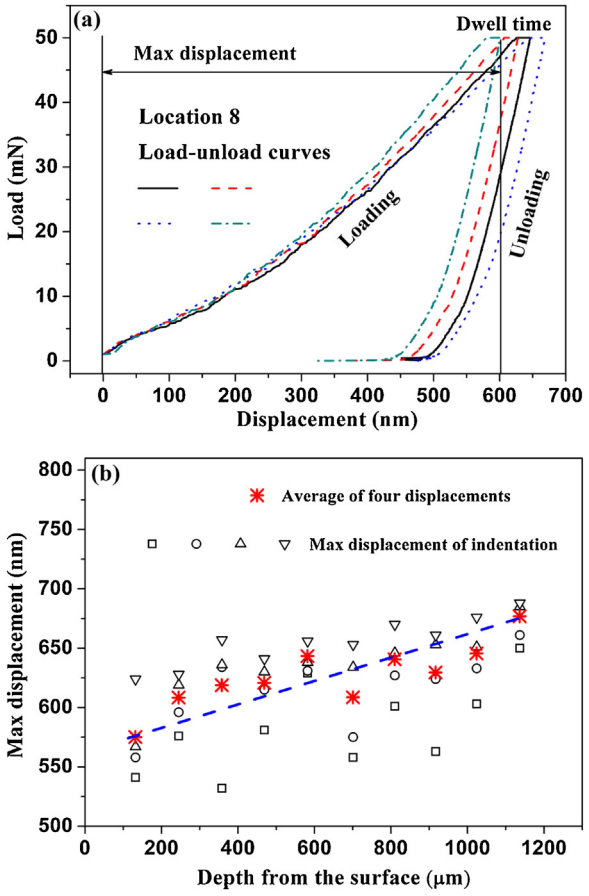

Fig. 5 – (a) Load-displacement curves of four indentations in location 8 as a representative location; (b) Maximum displacements calculated from the load-displacement curves with different depth from the surface.

3.2. *Investigation on hardness and reduced modulus*

Fig. 5(a) shows the load-displacement curves of four indentations in location 8 as a representative location. Each curve in the figure contains three parts, the loading phase, the dwell time with the maximum loading, and the unloading phase. During the calculation of the maximum displacement, the zero point is determined from the position where the load increases sharply, as shown in the figure. From all load-displacement curves, the net values of maximum displacement for ten different locations can be calculated, and the results are shown in Fig. 5(b). Moreover, in order to know more about the variation trend of displacements, the average displacement of four indentations in each location is also shown. From the figure, it is indicated that the maximum displacement increases gradually with the increase in depth, which is consistent with the size of indentation in Fig. 4(a) and can indirectly reveal the decrease of hardness. The average

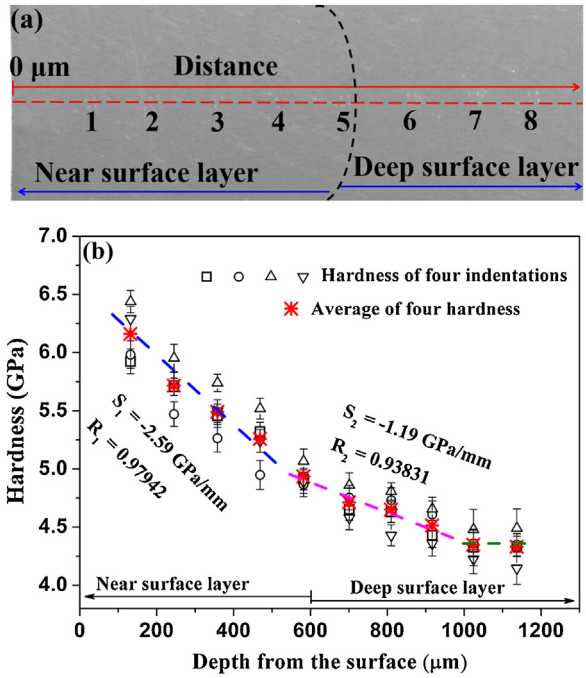

Fig. 6 – (a) The approximate boundary between the near surface layer and the deep surface layer; (b) Accurate and average values of hardness obtained from all load-displacement curves.

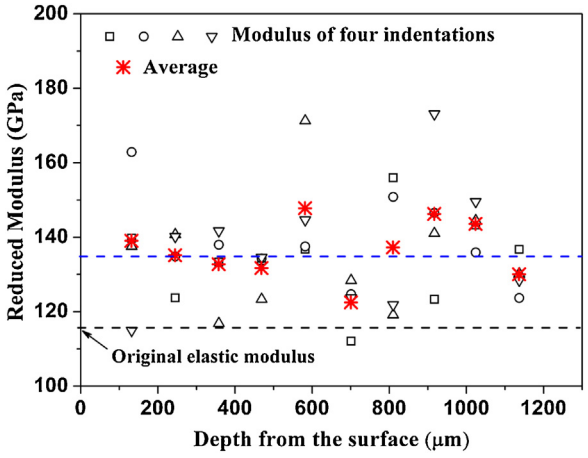

Fig. 7 – Accurate and average values of elastic modulus obtained from all load-displacement curves.

displacement increases from 572 nm (in location 1) to 671 nm (in location 10), which agrees with the variation of hardness in Fig. 6.

During the process of hardness measurement, four measurements are carried out at each location along the centerline, and four hardness values (*H*) are obtained. Fig. 6(a) shows the approximate boundary between the near surface layer and the deep surface layer. The accurate and average values of hardness are shown in Fig. 6(b). The error bars are obtained with a standard practice. In Fig. 6(b), the hardness decreases gradually with the increase in depth. And the maximum hardness appears at the depth of 132 μm (location 1), and the value is 6.438 ± 0.095 GPa, about 43% higher than the value (4.491 ± 0.165 GPa) at the depth of 1137 μm (location 10). In addition, the average hardness varies from 6.159 to 4.934 GPa in the near surface layer, which is much higher than the original hardness of Ti-6Al-4V (about 4.0 GPa). In the deep surface layer, the range of average hardness is 4.712 – 4.330 GPa, lower than those in the near surface layer, but still slightly higher than the original value. The hardness obtained by nanoindentaion method in this work is in accordance with pervious references [32,33,38]. In Ref. [32], the hardness range of Ti-6Al-4V was 4.09–4.71 GPa. In Li et al.'s work, nanoindentation tests identified a 15–20 μm thick of high hardness subsurface layer with peak hardness over 9 GPa in high-throughput drilling of Ti–6Al–4V, relative to the 4–5 GPa of bulk material [33]. In Cai et al.'s work, the influence of loading speed on micro hardness was studied and the hardness varied from 4.0 to 5.5 GPa with the variation of indenter displacement [38]. Based on the comparing and discussion, it can be found that the hardness obtained in the plastic zone is higher than that in the references, which may be caused by the plastic deformation and working hardening during loading.

In Fig. 6(b), the hardness in the near surface layer is higher than that in the deep surface layer. Moreover, the decline rate of hardness can be obtained from the relationship between hardness and depth. Based on the calculation and fitting, the relationship between hardness and depth is linear, and the slopes of the linear fits and their R-squared values are $S_1 = -2.59$ GPa/mm and $R_1 = 0.97942$ in the near surface layer, and $S_2 = -1.19$ GPa/mm and $R_2 = 0.93831$ in the deep surface layer. The decrease of hardness in the near surface layer is faster than that in the deep surface layer. In the process of high-load spherical indentation, the extent of deformation under the residual imprint is different through different layers of the material. The work hardening in the deep surface layer (600–1200 μm) is less than that in the near surface layer (0–600 μm), which is due to the plastic strain gradient imposed by loading of the large spherical ball. According to the theoretical work on contact mechanics, the maximum strain appears in the substrate, which is related to the contact radius of the indentation. However, the hardness is not proportional to the strain, and the hardness is influenced by some other factors. In this work, the max hardness appears under the ball indentation, but it is not on the accurate position of the contact radius, which may be ascribed to that the severe plastic deformation resulting in the work-hardening on the surface layer. Although the maximum hardness is not located on the accurate position of the contact radius, the variation trend of hardness can be shown and illuminated.

According to the Oliver–Pharr method [23], the reduced modulus can be obtained from the load-displacement curves and all results have been displayed in Fig. 7. The average reduced modulus have also been calculated and shown. It can be found that the scatter of the test results, but the average values doesn't vary a lot. And the average results vary around 135 GPa, which is higher than the original elastic modulus (114 GPa) tested by the conventional stress-strain method. The improvement of reduced modulus in the surface layer is resulted from the influence of different indentation sites during testing. Because Ti-6Al-4V contains two phases, the size

of indentation is small. Sometimes, the indenter impacts on only α phase, which results in the bigger modulus than the original modulus. Meanwhile, the average reduced modulus is also improved.

Based on the above analyses and the test results, the depth of local plastic zone below the residual imprint can be obtained and the approximate value is estimated to be 1100 μm. The severe plastic deformation is introduced due to the pressure and extrusion by 52,100 steel ball. Although the maximum hardness is not located on the accurate position of the contact radius, the variation trend of hardness can be shown and illuminated. Because of the effect of pressure and extrusion, the process of high-load spherical indentation is an essential process of work-hardening, which can induce the strain gradient below and around the residual imprint, and result in the improvement of hardness in the local plastic zone.

4. Conclusions

The variations of hardness and reduced modulus on the local plastic zone of Ti-6Al-4V were investigated via the nanoindentation method after implementing spherical loading. The results revealed that the hardness decreased gradually with the increase in depth, and the decrease rate in the near surface layer was faster than that in the deep surface layer, which was attributed to the plastic strain gradient imposed by loading of the large spherical ball. The maximum hardness was measured at the depth of 132 μm, and the value was 6.438 ± 0.095 GPa, about 43% higher than the value (4.491 ± 0.165 GPa) at the depth of 1137 μm. The average reduced modulus was about 135 GPa, which was higher than the original value. The improvement of reduced modulus was resulted from the influence of different indentation sites during testing. Based on the results, the depth of local plastic zone below the residual imprint was estimated as 1100 μm. The improvement of hardness in the local plastic zone were caused by the pressure and extrusion of 52,100 steel ball, which was an essential process of work-hardening and induced the plastic strain gradient below and around the residual imprint. Regarding the microstructure, the indenters impacted on both α and β phases, and the tested hardness were the average values of α and β phases.

Conflicts of interest

The authors declare no conflicts of interest.

Acknowledgments

This work was financial supported by Fundamental Research Funds for the Central Universities (WUT 2018IVA063, WUT 2018IVA064), “Chu Tian Scholar” project of Hubei Province (CTXZ2017-05), and the 111 Project (B17034). Thanks to National Science Foundation (Grant No. 51674167, 51504152, 51502142) and 973 Program (Grant no. 2014CB046701).

REFERENCES

[1] Zhang LC, Chen LY. A Review on Biomedical Titanium Alloys: Recent Progress and Prospect. Adv Eng Mater 2019;21(4), 1801215.
[2] Ma F, Wang C, Liu P, Li W, Liu X, Chen X, et al. Microstructure and mechanical properties of Ti matrix composite reinforced with 5 vol.% TiC after various thermo-mechanical treatments. J Alloys Compd 2018;758:78–84.
[3] Zhang LC, Liu Y, Li S, Hao Y. Additive manufacturing of titanium alloys by electron beam melting: a review. Adv Eng Mater 2018;20(5):1700842.
[4] Ma F, Lu S, Liu P, Li W, Liu X, Chen X, et al. Evolution of strength and fibers orientation of a short-fibers reinforced Ti-matrix composite after extrusion. Mater Des 2017;126:297–304.
[5] Ma F, Liu P, Li W, Liu X, Chen X, Zhang K, et al. The mechanical behavior dependence on the TiB whisker realignment during hot-working in titanium matrix composites. Sci Rep 2016;6:36126.
[6] Xie L, Wang L, Wang K, Yin G, Fu Y, Zhang D, et al. TEM characterization on microstructure of Ti-6Al-4V/Ag nanocomposite formed by friction stir processing. Materialia 2018;3:139–44.
[7] Davies PS, Wynne BP, Rainforth WM, Thomas MJ, Threadgill PL. Development of microstructure and crystallographic texture during stationary shoulder friction stir welding of Ti-6Al-4V. Metall Mater Trans A 2011;42(8):2278–89.
[8] Kabir ASH, Cao X, Gholipour J, Wanjara P, Cuddy J, Birur A, et al. Effect of postweld heat treatment on microstructure, hardness, and tensile properties of laser-welded Ti-6Al-4V. Metall Mater Trans A 2012;43(11):4171–84.
[9] Pilchak AL, Norfleet DM, Juhas MC, Williams JC. Friction stir processing of investment-cast Ti-6Al-4V: microstructure and properties. Metall. Mater. Trans. A 2007;39(7):1519–24.
[10] Nalla RK, Ritchie RO, Boyce BL, Campbell JP, Peters JO. Influence of microstructure on high-cycle fatigue of Ti-6Al-4V: bimodal vs. Lamellar structures. Metall Mater Trans A 2002;33(3):899–918.
[11] Yang YC, Chang E. Influence of residual stress on bonding strength and fracture of plasma-sprayed hydroxyapatite coatings on Ti-6Al-4V substrate. Biomaterials 2001;22(13):1827–36.
[12] Lee H, Mall S. Stress relaxation behavior of shot-peened Ti-6Al-4V under fretting fatigue at elevated temperature. Mater Sci Eng A 2004;366(2):412–20.
[13] Romero J, Attallah MM, Preuss M, Karadge M, Bray SE. Effect of the forging pressure on the microstructure and residual stress development in Ti-6Al-4V linear friction welds. Acta Mater 2009;57(18):5582–92.
[14] Fu Y, Loh NL, Batchelor AW, Liu D, Xiaodong Z, He J, et al. Improvement in fretting wear and fatigue resistance of Ti-6Al-4V by application of several surface treatments and coatings. Surf Coat Technol 1998;106(2–3): 193–7.
[15] Nalla RK, Altenberger I, Noster U, Liu GY, Scholtes B, Ritchie RO. On the influence of mechanical surface treatments—deep rolling and laser shock peening—on the fatigue behavior of Ti-6Al-4V at ambient and elevated temperatures. Mater Sci Eng A 2003;355(1–2):216–30.
[16] Golden PJ, Hutson A, Sundaram V, Arps JH. Effect of surface treatments on fretting fatigue of Ti-6Al-4V. Int J Fatigue 2007;29(7):1302–10.
[17] Xie L, Zhou Q, Jin X, Wang Z, Jiang C, Lu W, et al. Effect of reinforcements on rolling contact fatigue behaviors of titanium matrix composite (TiB + TiC)/Ti-6Al-4V. Int J Fatigue 2014;66:127–37.

[18] Zhou Q, Xie L, Wang X, Jin X, Wang Z, Wang J, et al. Modeling rolling contact fatigue lives of composite materials based on the dual beam FIB/SEM technique. Int J Fatigue 2016;83(Part 2):201–8.
[19] Xie L, Palmer D, Otto F, Wang Z, Jane Wang Q. Effect of surface hardening technique and case depth on rolling contact fatigue behavior of alloy steels. Tribol Trans 2015;58(2):215–24.
[20] Wagoner Johnson AJ, Bull CW, Kumar KS, Briant CL. The influence of microstructure and strain rate on the compressive deformation behavior of Ti-6Al-4V. Metall Mater Trans A 2003;34(2):295–306.
[21] Tjong SC, Ma Z. Microstructural and mechanical characteristics of in situ metal matrix composites. Mater. Sci. Eng., R 2000;29(3):49–113.
[22] Xie L, Wen Y, Zhan K, Wang L, Jiang C, Ji V. Characterization on surface mechanical properties of Ti-6Al-4V after shot peening. J Alloys Compd 2016;666:65–70.
[23] Oliver WC, Pharr GM. Improved technique for determining hardness and elastic modulus using load and displacement sensing indentation experiments. J Mater Res 1992;7(6):1564–83.
[24] Oliver WC, Pharr GM. Measurement of hardness and elastic modulus by instrumented indentation: advances in understanding and refinements to methodology. J Mater Res 2004;19(01):3–20.
[25] Doerner MF, Nix WD. A method for interpreting the data from depth-sensing indentation instruments. J Mater Res 1986;1(4):601–9.
[26] Nix WD. Mechanical properties of thin films. Metall Trans A 1989;20(11):2217–45.
[27] Tirupataiah Y, Sundararajan G. On the constraint factor associated with the indentation of work-hardening materials with a spherical ball. Metall Trans A 1991;22(10):2375–84.
[28] Pharr GM, Oliver WC. Measurement of thin film mechanical properties using nanoindentation. MRS Bull 1992;17(07):28–33.
[29] Saha R, Nix WD. Effects of the substrate on the determination of thin film mechanical properties by nanoindentation. Acta Mater 2002;50(1):23–38.
[30] Bhattacharya AK, Nix WD. Finite element analysis of cone indentation. Int J Solids Struct 1991;27(8):1047–58.
[31] Donohue BR, Ambrus A, Kalidindi SR. Critical evaluation of the indentation data analyses methods for the extraction of isotropic uniaxial mechanical properties using finite element models. Acta Mater 2012;60(9):3943–52.
[32] Han F, Tang B, Kou H, Li J, Feng Y. Experiments and crystal plasticity finite element simulations of nanoindentation on Ti-6Al-4V alloy. Mater Sci Eng A 2015;625:28–35.
[33] Li R, Riester L, Watkins TR, Blau PJ, Shih AJ. Metallurgical analysis and nanoindentation characterization of Ti-6Al-4V workpiece and chips in high-throughput drilling. Mater Sci Eng A 2008;472(1–2):115–24.
[34] Everitt NM, Ding J, Bandak G, Shipway PH, Leen SB, Williams EJ. Characterisation of fretting-induced wear debris for Ti-6Al-4V. Wear 2009;267(1–4):283–91.
[35] Man HC, Bai M, Cheng FT. Laser diffusion nitriding of Ti-6Al-4V for improving hardness and wear resistance. Appl Surf Sci 2011;258(1):436–41.
[36] Gong X, Lydon J, Cooper K, Chou K. Microstructural analysis and nanoindentation characterization of TI-6AL-4V parts from electron beam additive manufacturing. In: Proceedings of the ASME 2014 International Mechanical Engineering Congress and Exposition; 2014. p. 1–8.
[37] Kumaraswamy A, Vasudeva Rao V. High strain-rate plastic flow behavior of Ti-6Al-4V from dynamic indentation experiments. Mater Sci Eng A 2011;528(3):1238–41.
[38] Cai J, Li F, Liu T, Chen B. Investigation of mechanical behavior of quenched Ti-6Al-4V alloy by microindentation. Mater Charact 2011;62(3):287–93.
[39] Dong J, Li F, Wang C. Micromechanical behavior study of α phase with different morphologies of Ti-6Al-4V alloy by microindentation. Mater Sci Eng A 2013;580:105–13.
[40] Branch NA, Subhash G, Arakere NK, Klecka MA. Material-dependent representative plastic strain for the prediction of indentation hardness. Acta Mater 2010;58(19):6487–94.
[41] Branch NA, Arakere NK, Subhash G, Klecka MA. Determination of constitutive response of plastically graded materials. Int J Plast 2011;27(5):728–38.